Computer Methods and Programs in Biomedicine 260 (2025) 108530

Contents lists available at ScienceDirect

Computer Methods and Programs in Biomedicine

journal homepage: www.sciencedirect.com/journal/computer-methods-and-programs-in-biomedicine

Dependence of acoustophoretic aggregation on the impedance of microchannel's walls

Yiming Li [a], Dongfang Liang [a,*], Alexandre Kabla [a], Yuning Zhang [b], Jun Ma [a,c], Xin Yang [d]

[a] Department of Engineering, University of Cambridge, Cambridge, CB2 1PZ, UK
[b] Key Laboratory of Power Station Energy Transfer Conversion and System (Ministry of Education), School of Energy Power and Mechanical Engineering, North China Electric Power University, Beijing, 102206, China
[c] CHN Energy Technology & Economics Research Institute, Beijing Changping District Future Science City Shenhua Research Institute, Beijing, 102211, China
[d] School of Engineering, Cardiff University, Cardiff, CF24 3AA, UK

ARTICLE INFO

Keywords:
Microfluidics
Acoustofluidics
Acoustophoresis
Surface acoustic waves
Microchannels

ABSTRACT

Background and Objectives: Acoustofluidic manipulation of particles and biological cells has been widely applied in various biomedical and engineering applications, including effective separation of cancer cell, point-of-care diagnosis, and cell patterning for tissue engineering. It is often implemented within a polydimethylsiloxane (PDMS) microchannel, where standing surface acoustic waves (SSAW) are generated by sending two counter-propagating ultrasonic waves on a piezoelectric substrate.

Methods: In this paper, we develop a full cross-sectional model of the acoustofluidic device using finite element method, simulating the wave excitation on the substrate and wave propagation in both the fluid and the microchannel wall. This model allows us to carry out extensive parametric analyses concerning the acoustic properties of the fluid and the microchannel wall, as well as the dimensions of the channel, to explore their influences on the acoustic field, fluid flow and microparticle aggregation.

Results: Our findings demonstrate an order-of-magnitude enhancement in acoustic pressure amplitude and aggregation speed and a reduction in the particle threshold radius to submicron levels, which can be achieved through adjustments to the channel height and the difference in acoustic impedance between the channel wall and the fluid. The optimum channel heights are determined, which depend on the acoustic properties of the channel wall. The particle trajectories, movements along pressure nodal planes, and terminal positions are identified, with relative strength between the radiation force and the streaming force compared in different combinations of parameters.

Conclusions: This work demonstrates that finetuning the dimensions and acoustic properties of the fluid and microchannel wall in acoustofluidic device can greatly enhance particle aggregation throughput and reduce constraints on particle size. Our findings offer valuable insights into device design and optimization.

1. Introduction

Microfluidics, an emerging technology that manipulates small volumes of fluids and particles within micro-scale channels, has great potential in revolutionizing various fields, including biological analysis [1–4], medical diagnostics [5,6], and chemical synthesis [7,8]. In microfluidic particle manipulation, the drag force induced by the fluid flow is the primary driving force. To enhance the efficiency, sensitivity, and applicability of microfluidic technology, novel methods have been developed by integrating different physical fields with microfluidics, such as electrofluidics [9], acoustofluidics [10], thermofluidics [11], magnetofluidics [12]. These coupled approaches allow for tailored driving forces suited to specific applications. Among these methods, acoustofluidics, leveraging ultrasonic waves to actuate fluids and manipulate particles and cells, offers precise and contactless control within the microchannel. This technique has demonstrated capabilities in multiple applications, including aggregation and enrichment of micro- and nanoparticles [13–15], controllable translation, rotation and deformation of single cell or multiple cells [16,17], separation of circulating tumour cells [18,19], isolation of exosomes [20], and mixing of two fluids [21].

In typical acoustofluidic devices, ultrasonic waves are generated by

* Corresponding author.
E-mail address: dl359@cam.ac.uk (D. Liang).

https://doi.org/10.1016/j.cmpb.2024.108530
Received 1 August 2024; Received in revised form 25 November 2024; Accepted 25 November 2024
Available online 28 November 2024

the periodic vibration of transducers on piezoelectric materials at frequencies of applied electrical signals. Based on the wave propagation characteristics, the acoustic wave utilized in acoustofluidic devices can be categorized into two types [22]: bulk acoustic wave (BAW), which propagates through the entire volume of the piezoelectric medium, and surface acoustic wave (SAW), which is confined to the surface of the piezoelectric substrate. Since both the fluid and the channel wall material serve as media for acoustic waves propagation, the acoustic properties of the wall material and the dimensional parameters adopted in acoustofluidic devices are crucial for effective acoustophoretic particle manipulation. For a BAW-based device, it requires an acoustically hard channel wall material (e.g., silicon or glass) to reflect the bulk waves that travel through the fluid, thereby forming a resonant acoustic field with enhanced acoustic performance. Muller *et al.* [23] presented a 2D numerical study of acoustophoretic particle aggregation based on a typical BAW-based device with a silicon substrate and Pyrex lid, thoroughly investigating the transition in particle motions between acoustic-streaming-dominance swirling and radiation-force-dominance focusing. In contrary to common hard materials, Leibacher *et al.* [24] innovatively added an additional PDMS layer with acoustic impedance matched to the fluid, enabling flexible and controllable placement of pressure nodal planes. To enhance the performance of acoustophoretic particle manipulation, Şahin *et al.* [25] and Sanaz *et al.* [26] summarized the influences of various key operating and design parameters using a three-dimensional numerical model, and Açıkgöz *et al.* [27] investigated the effects of four commonly used chip materials. In addition to the conventional method of directly bonding microfluidic chambers onto the substrate, disposable microchannels made of glass [28] or PDMS [29] have been used for separating microparticles, with systematic studies reporting the resulting acoustofluidic patterning inside. For a SAW-based device, unlike the standing waves formed by the interference of incident and reflected waves within the bulk fluid, standing waves are generated by the superposition of two counter-propagating SAWs induced by a pair of interdigital transducers (IDTs) on the surface of the piezoelectric substrate. Based on Huygens-Fresnel principle [30], acoustic waves leak from the substrate into the overlaying fluid at a Rayleigh angle, interfering with the spherical wavelets induced along the propagation path of the wavefronts. To uncover the complex wave propagation mechanism in SAW-based devices, Collins *et al.* [31] described the interference of wavefronts and the resultant distribution of the acoustic field within the fluid for all channel wall and SAW orientations, while also determining the periodicity of the interference pattern. O'Rorke *et al.* [32] further developed a meshfree analytical model of the resultant acoustic field induced by the bottom-driven SAW, neglecting the reflections from the channel wall. Building on the development of analytical models for simple cases, a novel wave-number spiral acoustic tweezer was designed to dynamically reconfigure the SAW field into desired patterns, enabling precise and controllable particle manipulation [33]. Considering how acoustic waves couple with the fluid and channel, soft polymer materials (e.g. PDMS or polymethyl methacrylate) with low acoustic impedance and high damping are typically adopted as channel wall materials to prevent unwanted reflections and standing waves that may interfere with the desired acoustic field. Although hard materials have better acoustic performance, soft materials offer great biocompatibility, ease of fabrication, and high cost-effectiveness.

In SAW-based devices, acoustic waves emanate from the bottom and travel upwards until they are reflected back at the upper channel wall, resulting in a pseudo-standing wave (PSW) in the vertical direction. PSW is a combination of a travelling wave and a smaller-amplitude standing wave. Due to the poor acoustic properties of soft materials, many researchers have focused on developing novel methods to improve acoustic performance. Some have optimized operational and design parameters, while others have explored ways to enhance acoustic resonance in the vertical direction. Li *et al.* [34] investigated the influence of channel height on the acoustic pressure field and particle aggregation, where a generalized formula for the optimum channel height to achieve highest manipulation efficiency was determined. Wang *et al.* [35] replaced the upper channel wall with acoustic actuators (i.e., IDT for generating SAW or piezoelectric transducer for generating BAW), which worked simultaneously with the bottom-driven SSAW to actuate the fluid cavity sandwiched in between. Their results showed significant improvements in particle velocity and manipulation throughput compared to conventional device configurations. Without involving more transducers, Wu *et al.* [36,37] demonstrated an innovative acoustofluidic tweezer with a glass layer placed between the upper PDMS wall and the fluid to increase the acoustic impedance mismatch, thereby a stronger set of standing waves is formed in the vertical direction. Their device has successfully enabled high-throughput micro- and nano- particle/cell alignment and separation, highlighting the significant impact of channel wall material on the acoustic pressure field and acoustophoretic manipulation. By tailoring the standing wave component of the vertical PSW through adjusting the acoustic impedance discrepancies between the upper channel wall and the fluid, particle aggregation can be accelerated, and particle alignment positions can be adjusted accordingly.

However, to the best of the authors' knowledge, few studies have systematically investigated the influence of acoustic impedance mismatch between the upper channel wall and the fluid on particle manipulation in a SAW-based device. Therefore, in this paper, we shed light on the influences of impedance mismatch on the distribution and amplitude of the acoustic pressure and flow field, trajectories and terminal positions of particle, efficiency of particle aggregation, and sensitivity to particle size. To facilitate our study, we developed a full cross-sectional model based on finite element method (FEM), which accounts for acoustic actuation on the piezoelectric substrate and wave propagation in both the channel wall and the fluid. We also consider the effects of channel height, as it is an important parameter affecting the distance that waves travel upwards until reflection at the upper wall. The generic formula for optimum channel height determined in our previous study is further refined to incorporate the influence of the impedance mismatch. These studies provide guidelines for channel material selection and the design of SSAW-based devices.

2. Methods

2.1. SSAW acoustofluidic system and governing equations

2.1.1. SAW propagation in piezoelectric solids

In modelling the propagation of ultrasonic waves in a piezoelectric substrate, the electrical excitation and mechanical motion are coupled, with anisotropic properties. The linear constitutive relationship for a piezoelectric material in the stress-charge form consist of two equations. One is the charge conservation equation for the electrical field, derived from Maxwell's equations, and the other is the momentum equation, describing the mechanical motion: [38]

$$\sigma_{ij} = c_{ijkl} S_{kl} + e_{kij} E_k, \tag{1}$$

$$D_i = e_{ikl} S_{kl} + \varepsilon_{ij} E_k, \tag{2}$$

where σ_{ij} is the mechanical stress tensor, c_{ijkl} is the elasticity matrix, S_{kl} is the strain tensor, e_{kij} is the piezoelectric matrix, E_k is the electrical field vector, D_i is the electrical displacement vector, and ε_{ij} is the permittivity tensor. Given that the solid deformation is caused by small acoustic disturbances, the relationship between the strain S_{kl} and displacement u_k can be given by:

$$S_{kl} = \frac{1}{2}(\partial_k u_l + \partial_l u_k) \tag{3}$$

Cauchy's wave equation for a viscoelastic, homogeneous and anisotropic piezoelectric solid, when disregarding body forces, relates the

mechanical displacement u_i and stress σ_{ij} as follows: [39,40]

$$\partial_i \sigma_{ij} = \rho_s \ddot{u}_i, \tag{4}$$

where ρ_s is the mass density of the solid. The electrical field can be determined under quasi-static assumption as the electromagnetic disturbances propagate much more rapidly than the elastic ones. Therefore, Maxwell's equation can be simplified to be $\nabla \times E = 0$, implying that the electrical field E_k is irrotational and can be expressed by the negative gradient of a scalar electrical potential field ϕ as:

$$E_k = -\partial_k \phi. \tag{5}$$

As the piezoelectric solid acts as a perfect dielectric material with no free charge on their surface, the electrical displacement D_i is governed by Gauss's Law: [39,40]

$$\partial_i D_i = 0. \tag{6}$$

Incorporating Eqs. (2)-(6) into Eq. (1), the coupled linear constitutive equations for SAW traveling in a piezoelectric substrate are derived as:

$$\rho \ddot{u}_i = c_{ijkl} u_{k,lj} + e_{kij} \phi_{,kj}, \tag{7}$$

$$e_{ikl} u_{k,li} - \varepsilon_{ij} \phi_{,ji} = 0. \tag{8}$$

2.1.2. SAW propagation in viscoelastic solids

For the microchannel wall composed of a viscoelastic and isotropic solid, such as PDMS, it can be deemed as quiescent fluid, meaning that there are no shear waves within the channel wall. The assumption can be justified by the extremely small shear modulus and significant acoustic attenuation of the materials like PDMS. The harmonic acoustic field therein is governed by the Helmholtz equation, which accounts for acoustic attenuation and wave leakage at the substrate-PDMS interface and at the fluid-PDMS interface:

$$\nabla \cdot \left(-\frac{1}{\rho_{\mathrm{PDMS}}} \nabla p_{\mathrm{PDMS}} \right) - \frac{k^2 p_{\mathrm{PDMS}}}{\rho_{\mathrm{PDMS}}} = 0, \tag{9}$$

where p is the acoustic pressure within the PDMS channel wall, and the wave number k is defined to be:

$$k = \frac{\omega}{c_{\mathrm{L}}} - i\left[\frac{\ln(10)}{20}\alpha_{\mathrm{s}}\right], \tag{10}$$

where α_s is the attenuation coefficient of acoustic waves in the wall, c_L is the speed of the longitudinal waves in the wall, ω is the angular frequency, and i stands for the imaginary unit.

2.1.3. Acoustically induced fluid dynamics

Inside the channel, the fluid motion induced by acoustic waves is governed by the Navier-Stokes equation and the continuity equation. The fluid is assumed to be Newtonian and compressible. Implementing the perturbation method [41], the fluid motion is decomposed into the zeroth-order quiescent component, the first-order time harmonic component, and second-order component. The first-order component represents the periodic responses to acoustical excitation.

$$i\omega \rho_1 = -\rho_0 \nabla \cdot \boldsymbol{v}_1, \tag{11}$$

$$i\omega \rho_0 \boldsymbol{v}_1 = -\nabla p_1 + \mu \nabla^2 \boldsymbol{v}_1 + \left(\mu_{\mathrm{b}} + \frac{\mu}{3}\right) \nabla (\nabla \cdot \boldsymbol{v}_1), \tag{12}$$

where ρ, $\boldsymbol{v}$, p represent the fluid density, velocity, and pressure, respectively, and μ and μ_b are the shear viscosity and bulk viscosity, respectively. The subscripts 0 and 1 denote the zeroth- and first-order terms, respectively. For the second-order component, only the time-averaged streaming flow field is needed in the computation.

$$-\nabla \cdot \langle \rho_1 \cdot \boldsymbol{v}_1 \rangle = \rho_0 \nabla \cdot \langle \boldsymbol{v}_2 \rangle, \tag{13}$$

$$\left\langle \rho_1 \frac{\partial \boldsymbol{v}_1}{\partial t} \right\rangle + \rho_0 \langle (\boldsymbol{v}_1 \cdot \nabla) \boldsymbol{v}_1 \rangle = -\nabla \cdot \langle p_2 \rangle + \mu \nabla^2 \langle \boldsymbol{v}_2 \rangle + \left(\mu_{\mathrm{b}} + \frac{\mu}{3}\right) \nabla (\nabla \cdot \langle \boldsymbol{v}_2 \rangle), \tag{14}$$

where subscript 2 refers to the second-order perturbation term, and the angle brackets indicate the time-averaging over a period of oscillation.

2.1.4. Acoustophoretic forces and particle motions

The motion of a spherical particle suspended in a viscous fluid is primarily balanced by two forces: the acoustic radiation force and the Stokes drag force. Neglecting the interaction among particles, the time-averaged radiation force exerted on particles with radii much smaller than the acoustic wavelength can be expressed by [42,43]

$$\boldsymbol{F}_{\mathbf{rad}} = -\pi r^3 \left[\frac{2\kappa_0}{3} \mathrm{Re}\left[f_1^* p_1^* \nabla p_1 \right] - \rho_0 \mathrm{Re}\left[f_2^* \boldsymbol{v}_1^* \nabla \boldsymbol{v}_1 \right] \right], \tag{15a}$$

where κ_0 is the compressibility of the fluid, r is the particle radius, and the asterisk symbolizes the complex conjugate. The monopole scattering coefficient f_1 and dipole scattering coefficient f_2 are expressed as [43]

$$f_1 = 1 - \frac{\kappa_{\mathrm{p}}}{\kappa_0}, \tag{15b}$$

$$f_2 = \frac{2(1-\gamma)(\rho_{\mathrm{p}} - \rho_0)}{2\rho_{\mathrm{p}} + \rho_0 (1 - 3\gamma)}, \tag{15c}$$

$$\gamma = -\frac{3}{2}\left[1 + i\left(1 + \frac{\delta}{a}\right)\right]\frac{\delta}{a},\ \delta = \sqrt{\frac{2\mu}{\omega \rho_0}}, \tag{15d}$$

where ρ_p is the density of the particle, δ is the thickness of the viscous boundary layer, and γ is a variable dependent on δ. The time-averaged Stokes drag force, induced by the time-averaged acoustic streaming, is given by

$$\boldsymbol{F}_{\mathbf{drag}} = 6\pi \mu r \left(\langle \boldsymbol{v}_2 \rangle - \boldsymbol{v}_{\mathbf{p}} \right) \tag{16}$$

where $\boldsymbol{v}_{\mathbf{p}}$ is the particle velocity.

As the buoyancy and gravity forces are nearly cancelled out in practical applications, the particle trajectories can be obtained according to Newton's second law of motion:

$$m_{\mathrm{p}} \frac{\mathrm{d}(\boldsymbol{v}_{\mathbf{p}})}{\mathrm{d}t} = \boldsymbol{F}_{\mathbf{drag}} + \boldsymbol{F}_{\mathbf{rad}} \tag{17}$$

The inertial effects of microparticles can be safely neglected as the acceleration time is in the order of microseconds and the acceleration distance is much smaller than the particle size. Therefore, the particle velocity can be determined by setting the left-hand side of Eq. (17) to zero.

2.1.5. Acoustic energy

The total acoustic energy densities, averaged in both time and space, in the fluid, $\overline{E_{ac}^{fl}}$, and in the solid, $\overline{E_{ac}^{sl}}$, are defined as the sum of the kinetic and compressional energy densities and the sum of the kinetic and elastic energy densities, respectively, as given by [44,45]

$$\overline{E_{ac}^{fl}} = \frac{1}{V_{fl}} \int_{V_{fl}} \left(\frac{1}{2}\kappa_0 \langle p_1 p_1^* \rangle + \frac{1}{2}\rho_0 \langle \boldsymbol{v}_1 \boldsymbol{v}_1^* \rangle \right) dV_{fl}, \tag{18}$$

$$\overline{E_{ac}^{sl}} = \frac{1}{V_{sl}} \int_{V_{sl}} \left(\frac{1}{2}\rho_s \omega^2 \langle u_k u_k \rangle + \frac{1}{2} \langle S_{kl} \sigma_{kl} \rangle \right) dV_{sl}, \tag{19}$$

where V_{fl} and V_{sl} are the fluid volume and solid volume, respectively.

2.2. Numerical model

2.2.1. Model setup and boundary conditions

Fig. 1 illustrates a typical configuration of the SSAW-based acoustofluidic device for particle aggregation, consisting of a PDMS microchannel filled with water and a pair of metallic IDTs with electrode arrays bonded on the surface of a 128° $Y-X$ lithium niobate ($LiNO_3$) piezoelectric substrate. The substrate is 800μm in thickness and 6mm in width. The PDMS channel is 600μm high and 2.4mm wide, and the water cavity embedded in the PDMS has a fixed width of $w = 600\mu$m. Two IDTs, each equipped with two pairs of finger electrodes, are configured on opposite sides of the channel, with an IDT pitch of 300μm to allow megahertz SAW frequency. By applying harmonic electric signals of frequency f to the IDT electrodes, SSAWs are formed on the surface of the substrate and subsequently leaked into the PDMS channel and the water domain at a Rayleigh angle. We consider a long and straight microchannel. The primary movement of the particle-fluid mixture is in the longitudinal direction, x, of the channel. A 2D cross-sectional model over the x-z plane is established in Fig. 1 to capture the essential wave propagation, cross-sectional fluid flow, and particle dynamics in the transverse and vertical direction caused by the imposed ultrasonic waves.

The boundary conditions applied at corresponding interfaces are labelled in Fig. 1. An impedance boundary condition is prescribed on all external boundaries of the PDMS material in contact with the air, where the impedance of air J_{air} is used. Given that the amplitude of the SAW propagating on the surface of the substrate decays exponentially with a penetration depth of 1 to 2 wavelength into the substrate [46], low-reflecting boundary conditions are introduced at the bottom and lateral surfaces of the substrate to minimize reflections. A surface-free boundary condition is applied at the top surface of the substrate facing air. At the interfaces of the substrate, PDMS, and microchannel liquid, the continuity conditions are applied to ensure the smooth transitions of velocity and stress.

Polymer devices are extensively adopted as a means to reduce costs. However, the intrinsic acoustic properties of polymer-based devices are relatively poor and unsuitable to form acoustically resonant systems. The rapid acoustic energy losses in the polymer combined with the small difference in acoustic impedance from water result in a low Q factor. Contrary to the conventional acoustofluidic devices with PDMS channels in Fig. 1, we hereby propose novel configurations by adopting different wall materials to enhance acoustic resonance within the fluid. Intuitively, Fig. 2**(a)** demonstrates an acoustofluidic system with microchannel made from a material with significantly different impedance from that of water inside the channel, designated as material Z. Fig. 2**(b)** is distinguished by a channel lid made from material Z, bonded to the PDMS sidewalls. Fig. 2**(c)** adds a reflector placed at the top of the microchannel. These modifications, specifically equipping the device with a different channel wall material, a lid, or a reflector with a significant mismatch in acoustic impedance, may enhance acoustic resonance. These enhancements can lead to higher acoustic pressure, stronger the acoustic radiation force, and consequently, improved device performance. Therefore, we aim to explore the potential effects of

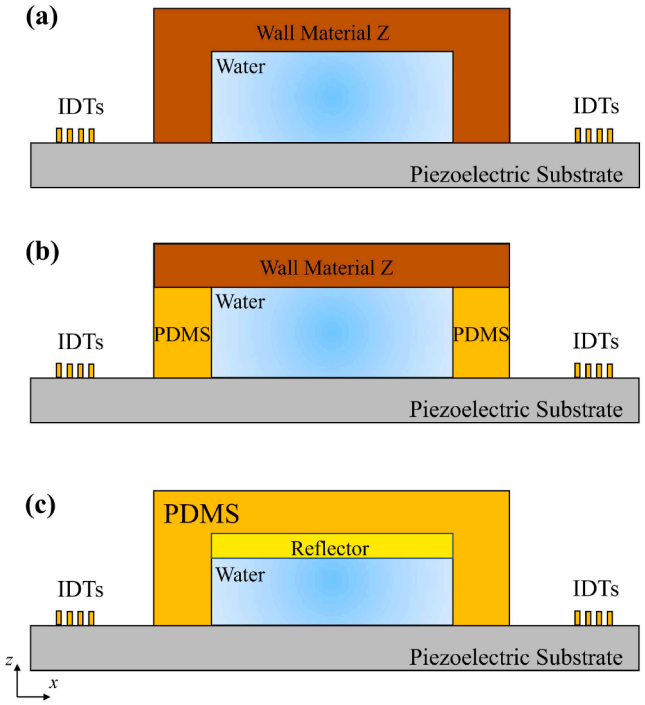

Fig. 2. The 2D sketch of novel SSAW-based acoustofluidic systems featuring (a) microchannel wall made from a specific material, labelled as material Z, (b) a channel lid composed of material Z and bonded on PDMS sidewalls, and (c) a reflector positioned between PDMS channel wall and the fluid cavity.

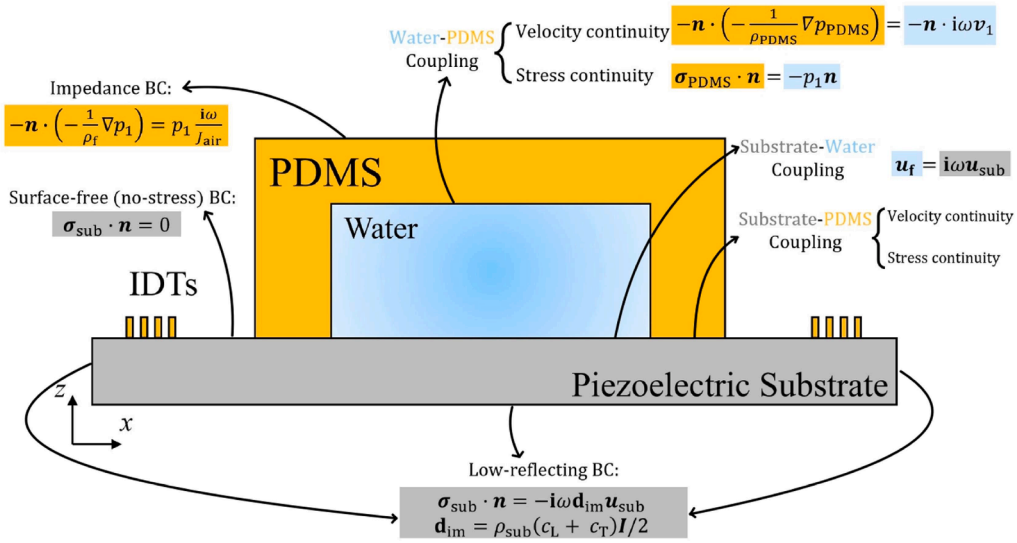

Fig. 1. Computational model of a typical acoustofluidic system, consisting of a PDMS domain (gold), water domain (blue), and piezoelectric solid (grey). Black arrows point to the boundary conditions corresponding to each interface.

the acoustic impedance discrepancy between the fluid and the channel wall material on the flow and particle movement, thereby identifying the optimal conditions for the efficient and accurate particle manipulation.

In our study, the acoustic wavelength is $\lambda_{SAW} = 600\mu$m, corresponding to frequency $f = 6.65$MHz. The input power applied on IDTs is 1 W, resulting in the displacement amplitude of the SAW $u_0 = 0.12$nm. In keeping the isothermal condition, the temperature is maintained at $T = 25\ ^{\circ}$C. The properties of water include its density $\rho_0 = 998$kg/m^3, longitudinal wave speed $c_0 = 1497$m/s, bulk viscosity $\mu_b = 2.47$mPas, shear viscosity $\mu = 0.89$mPas, and compressibility $\kappa_0 = 448$TPa^{-1}. The key parameters of polystyrene include its density $\rho_p = 1050$kg/m^3, longitudinal wave speed $c_p = 2350$m/s, and compressibility $\kappa_p = 249$TPa^{-1}. The key parameters of PDMS include its density $\rho_{PDMS} = 920$kg/m^{3}and longitudinal wave speed $c_{PDMS} = 1076.5$m/s. The key parameters of LiNbO3 are its density $\rho_{sub} = 4648$kg/m^3 and speed of sound $c_{sub} = 3994$m/s [47,48,49,50,51]. The elastic, dielectric, and piezoelectric matrices of the 128° $Y-X$ $LiNbO_3$ are taken to be the same as those specified in the COMSOL Multiphysics software.

2.2.2. Numerical implementation and validation

The governing equations of the acoustofluidic system and the corresponding boundary conditions are programmed and solved using the FEM computational package– COMSOL Multiphysics. The piezoelectric effects of the $LiNO_3$ substrate are modelled by coupling the "Electrostatics" and "Solid mechanics" modules in COMSOL. Here, the boundary condition for the IDTs is defined by specifying the terminal power in the "Terminal" node within the "Electrostatics" module. The terminal power, representing the input power supplied from the transmission lines to the IDTs, is always fixed at 1 W, so as to guarantee a fair comparison of the device efficiency when the channel height and lid material vary. The water flow inside the channel is analysed with the "Thermo-viscous Acoustics" module for first-order solutions and the "Laminar Flow" module for second-order solutions. The PDMS walls are treated as an absorptive non-flowing fluid, using the "Pressure Acoustics" module to simulate wave propagation and interference. To ensure the continuity of stress and velocity distributions through the domain interfaces, the "Multiphysics" module is used to bridge the physical properties across different modules. Furthermore, the "Particle Tracing for Fluid Flow" module is employed to trace and analyse particle trajectories and their final resting positions within the channel.

To accurately solve the equations in different physical domains, especially within the thin boundary layers of the flow field, the size of the triangular mesh elements is carefully chosen. The mesh convergence analysis examines the mesh dependence of some key parameters, including the acoustic pressure and velocity in the PDMS and water domains, SAW displacement in the substrate, and the streaming velocity in the water domain. According to the results from the mesh convergence analysis, to achieve adequate resolution, we need to set the maximum element size on the water side of the fluid-solid interface to be 0.3δ to capture the dynamics within the boundary layers, while the maximum mesh size is set to be 3δ at the centre of the water domain. In the $LiNO_3$ substrate, the maximum mesh size is $\lambda_{SAW}/15$, and in the PDMS domain, it is set to $\lambda_{PDMS}/10$, where the wavelength of longitudinal wave in PDMS is $\lambda_{PDMS} = c_{PDMS}/f$.

A representative simulation results for the conventional acoustofluidic setup are visualised in Fig. 3, capturing the spatial distributions of acoustic pressure in water and PDMS walls, as well as the SAW displacement in piezoelectric substrate. The water domain is marked by the white dotted line. By applying A/C electrical signals to the two symmetrically positioned IDTs, two identical counter-propagating SAWs are generated and superimpose with each other, forming a SSAW field in the central region of the substrate. While SAWs propagate through the PDMS-substrate and water-substrate interfaces, they partially radiate into the PDMS and water domains at a Rayleigh angle θ_R, as denoted in Fig. 3. As the leaky waves travel upwards in the water channel, they undergo attenuation and ultimately reflect upon reaching the PDMS-air and water-PDMS interfaces. Therefore, a SSAW field can be observed in the transverse direction of the microchannel, while a PSW field is formed in the vertical direction. Due to the approximate impedance matching between the fluid and the channel wall, the distributions of acoustic pressure in the water and PDMS domains exhibit periodic oscillation, which also matches displacement profile at the substrate surface. For model validation purpose, we conducted numerical simulations using operational and design parameters in line with Sun et al. [52]. The SAW displacement along the substrate surface exhibits a perfect sinusoidal profile with a wavelength of λ_{SAW} and a gradually decaying feature inside the substrate. Three pressure nodes (PNs) are introduced at the

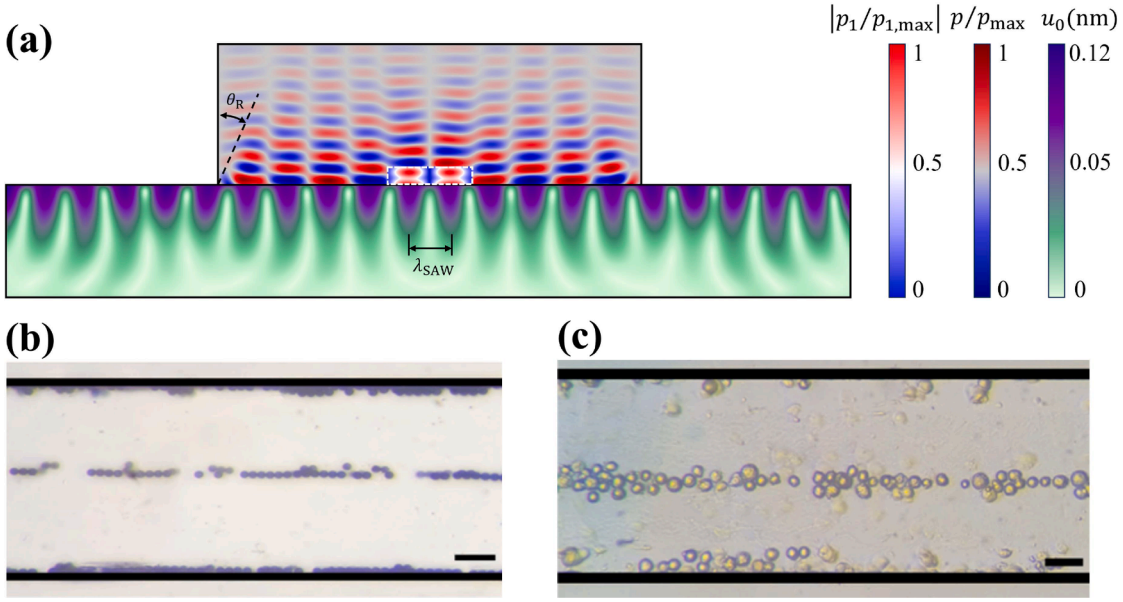

Fig. 3. Model verification between numerical and experimental results. (a) Numerical visualization of SAW displacement in $LiNO_3$ substrate and acoustic pressure distribution in water and PDMS domains. (b) Experimental results of 10-μm polystyrene microspheres patterning from Sun et al. [52] (c) Experimental results of biological cells patterning from Sun et al. [52]

central region of the channel and near the two sidewalls, which are the equilibrium positions for particle aggregation. The PNs simulated from our numerical model show good agreement with the experimental results from Sun et al. [52], as depicted in Fig. 3**(b)** and **(c)**, where three traces of aggregated particles and biological cells can be seen.

Fig. 4 illustrates the first-order acoustic pressure distribution, the streaming flow field, and particle velocity field within the fluid cavity enclosed by a hybrid channel with two PDMS sidewalls and a top lid composed of glass or silicon, and those by a uniform channel wall entirely made of glass or silicon. The hybrid setup is similar to the setup with a reflector at the top. Comparing with the model with PDMS channel wall in Fig. 3, the hybrid channel in Fig. 4**(a)** shows an upward shift in the elliptical acoustic resonance patterns, positioning the PNs of the vertical standing wave at $z = 60\mu$m and resulting in stronger standing waves. For the uniform glass/silicon channel in Fig. 4**(b)**, the elliptical patterns move towards the four corners of the rectangular channel, leading to a single PN at the centre and two pressure antinodes (ANs) near the sidewalls. Corresponding to the changes in the acoustic pressure distribution, the flow field adapts accordingly. The second-order acoustic streaming originates from the nonlinear effect of the acoustic oscillation within the fluid, as indicated by the nonlinear convective acceleration term $\rho_0\langle(v_1 \cdot \nabla)v_1\rangle$ in Eq. (14). The spatial gradient of first-order acoustic field plays a crucial role in the formation of acoustic streaming, and streaming vortices are normally formed between PNs and ANs. As the entire cavity is bounded by rigid, high-impedance materials (i.e., glass or silicon), acoustic waves are reflected more efficiently, leading to strong standing wave patterns and complex wave interference in the domain. Due to the nature of wave reflections at the interface of a high-impedance medium and a low-impedance medium, acoustic velocity maxima occur at boundaries, constraining the formation of stable streaming vortices. With steeper velocity gradient away from the sidewalls, two distinct streaming vortices can be observed between PNs and ANs. Considering the characteristics of the two setups, the hybrid one presents a regular acoustic field with higher amplitude and apparent horizontal and vertical pressure nodal and antinodal planes for particle aggregation. In contrast, the uniform channel setup displays a pressure distribution with a lower amplitude and a large low-pressure area where particle movement is slow, as shown in particle velocity vector field in Fig. 4**(b)**. The hybrid channel setup with PDMS sidewalls and a glass/silicon lid reaches strong acoustic resonance within the fluid and maintains an appropriate acoustic pressure distribution to facilitate particle aggregation. Therefore, the hybrid channel setup is desirable. In this work, we mainly focus on the influence of channel wall material on the particle aggregation in a hybrid channel setup.

3. Results

The acoustofluidic device is acoustically actuated through the bottom substrate and a proportion of the ultrasonic energy leaks into the microchannel walls and then the fluid, while the upper channel wall is passive. The acoustic properties of the microchannel walls play an important role in shaping the resultant acoustic wave field, greatly influencing the acoustophoretic performance. The conventional PDMS channel walls, whose acoustic impedance nearly matches that of water, still reflect a little amount of acoustic waves, resulting in PSWs, with small standing wave components in the vertical direction. By altering the material of the upper channel wall to increase the difference between its acoustic impedance mismatch and that of the fluid, reflections at the wall-fluid interface and the amplitude of PSWs in the vertical direction can be reinforced. Consequently, this adjustment can potentially enhance the total acoustic energy density stored in the bulk fluid, resulting in an increased radiation force that drives particles towards PNs. In this section, we employ the model setups in Fig. 2**(b)**, where the microchannel is fabricated by an upper wall made of material Z and two sidewalls made of PDMS. Since our focus is primarily on the physics within the fluid domain, only the results within the fluid cavity are presented in this section. Here, we thoroughly investigate the influence of channel height and the influence of the acoustic impedance discrepancy between the upper channel wall and the fluid on the flow field within the channel. The performance of particle aggregation is examined in terms of trajectories, terminal positions, efficiency, and threshold size, with an aim to identify the optimal operating conditions.

3.1. Acoustic field

The oscillating acoustic pressure field within channels of 120-μm and 180-μm in height, as shown in Fig. 5, depicts a clear standing wave with

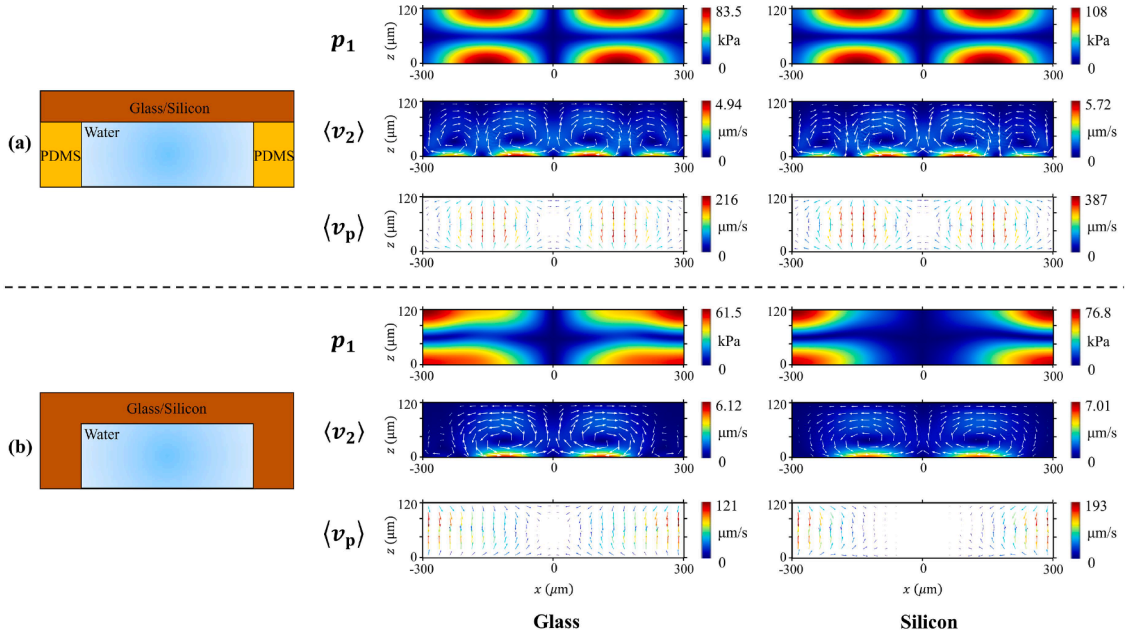

Fig. 4. Comparison of acoustic pressure, fluid flow, and particle velocity fields between acoustofluidic device configurations: (a) water cavity enclosed by a hybrid channel with PDMS sidewalls and a lid made from glass or silicon, and (b) water cavity enclosed by a uniform channel wall made from glass or silicon.

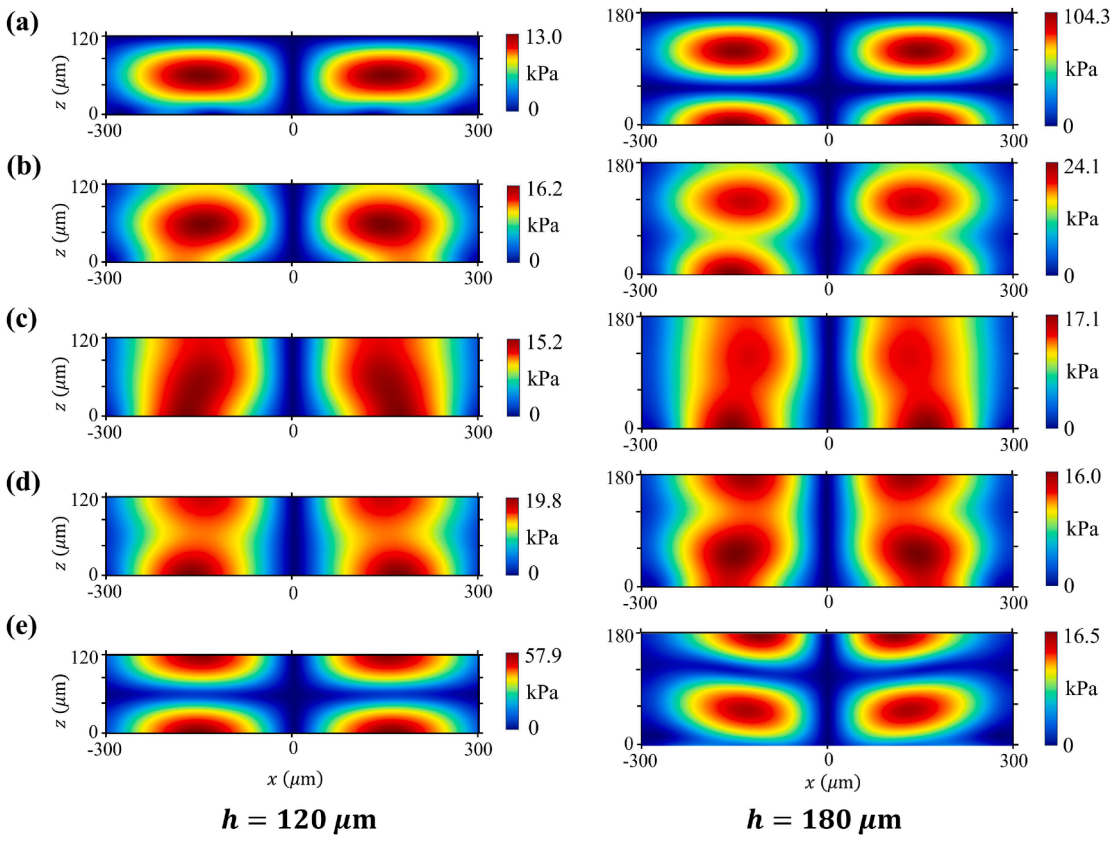

Fig. 5. Acoustic pressure distribution at channel height of $h = 120\mu$m and $h = 180\mu$m with the upper channel wall acoustic impedance of J^*= (a) 0.07, (b) 0.67, (c) 1, (d) 1.33, (e) 6.67.

periodic PNs and ANs formed in the horizontal direction. In the vertical direction, the acoustic wave patterns mainly depend on the acoustic radiation from the bottom and the wave reflection at the top. To facilitate our study, we introduce a non-dimensional parameter $J^* = J_{upp}/J_f$, which represents the ratio of the acoustic impedance of the upper channel wall to that of the fluid. In an idealized case that the acoustic impedance of the upper channel wall J_{upp} matches exactly that of the fluid J_f as shown in Fig. 5**(c)**, the acoustic pressure profile exhibits a columnar shape with similar standing waves observed at different height. Gradual attenuation can be observed vertically, as all upward waves are transmitted into and subsequently absorbed by the upper wall. Hence, the global pressure minima are located exclusively near horizontal PNs at sidewalls and centre of the channel (i.e., $x = 0, \pm 300\mu$m). For the case of a low impedance mismatch between the upper wall and the fluid, as presented in Fig. 5**(b)** and **(d)** where $J^* = 0.67$ and 1.33, respectively, PSW patterns emerge in the vertical direction with periodic PNs. This is because the incident acoustic waves are only slightly reflected from the upper wall, causing interference with the incident waves. Despite the presence of PNs in the vertical direction, they exert weaker influence than those along the horizontal direction, resulting in global pressure minima remaining at the PNs of the horizontal standing wave, as indicated by the dark blue areas in Fig. 5**(b)** and **(d)**. In contrast, for high acoustic impedance mismatch, as shown in Fig. 5**(a)** and **(e)** where $J^* = 0.07$ and 6.67, respectively, strong standing wave fields are captured in both the horizontal and vertical directions, as the majority of acoustic waves are reflected at the upper wall. The enhanced standing waves in the vertical direction lead to clear vertical PNs, resulting in the global pressure minima being located at the PNs of both vertical and horizontal standing waves. In addition, it is worth noting that there is a phase shift between the standing waves formed in the vertical direction in Fig. 5**(a)** and **(e)**, which can be attributed to the 180-degree phase difference between wave reflections caused by the sudden increase or decrease of acoustic impedance. This phase shift of the reflected waves causes a $\lambda_\perp/4$ discrepancy in the positions of PNs of the vertical standing wave, resulting in PNs of the vertical standing wave being positioned at $z = h - n\lambda_\perp/2$ for $J^* < 1$ and at $z = h - (2n+1)\lambda_\perp/4$ for $J^* > 1$ ($n = 0, 1, 2, \ldots$).

Figs. 6**(b)** and **(c)** demonstrate the variation in acoustic pressure amplitude as a function of channel height for the case of $J^* < 1$ and $J^* > 1$, respectively, where both present an oscillatory descending trend as channel height increases. For the case of $J^* < 1$ in Fig. 6**(b)**, specifically $J^* = 0.07$ and 0.67, the periodic presence of maximum acoustic pressure amplitude at specific channel height $h_{max,n}$ coincides well with our previously obtained results [34]. As reported in our previous study, for a PDMS microchannel filled with water (i.e., $J^* = 0.67 < 1$), the periodicity of the wave interference pattern in the vertical direction is determined as $\lambda_\perp = \lambda_{SAW}\tan[\sin^{-1}(\lambda_f/\lambda_{SAW})]$, and the channel heights that reach maximum acoustic pressure amplitude are captured at $h_{max,n} = (2n-1)\cdot\lambda_\perp/4$ to achieve constructive wave interference in the vertical direction. In contrast, for the case of $J^* = 6.67 > 1$ in Fig. 6**(c)**, the channel heights $h'_{max,n}$ that maximize acoustic pressure amplitude exhibit a $\lambda_\perp/4$ difference to $h_{max,n}$ due to the aforementioned $\lambda_\perp/4$ discrepancy in the positions of vertical PNs. Therefore, these specific channel heights for $J^* > 1$ can be summarized as $h'_{max,n} = h_{max,n} + \lambda_\perp/4 = n\lambda_\perp/2$.

Figs. 6**(a)** and 7 explain how the acoustic impedance of the upper wall affects the maximum acoustic pressure amplitude $p_{1,max}$ and the spatial average of the total acoustic energy density $\overline{E_{ac}^{fl}}$, respectively. As the acoustic impedance discrepancy between the upper wall and the fluid widens, the acoustic pressure amplitude is enhanced, which is especially significant at channel heights close to $h'_{max,n}$ or $h_{max,n}$. Specifically, with channel heights of $h'_{max,n}$ and $h_{max,n}$, the acoustic pressure amplitude in scenarios with a high impedance mismatch can achieve

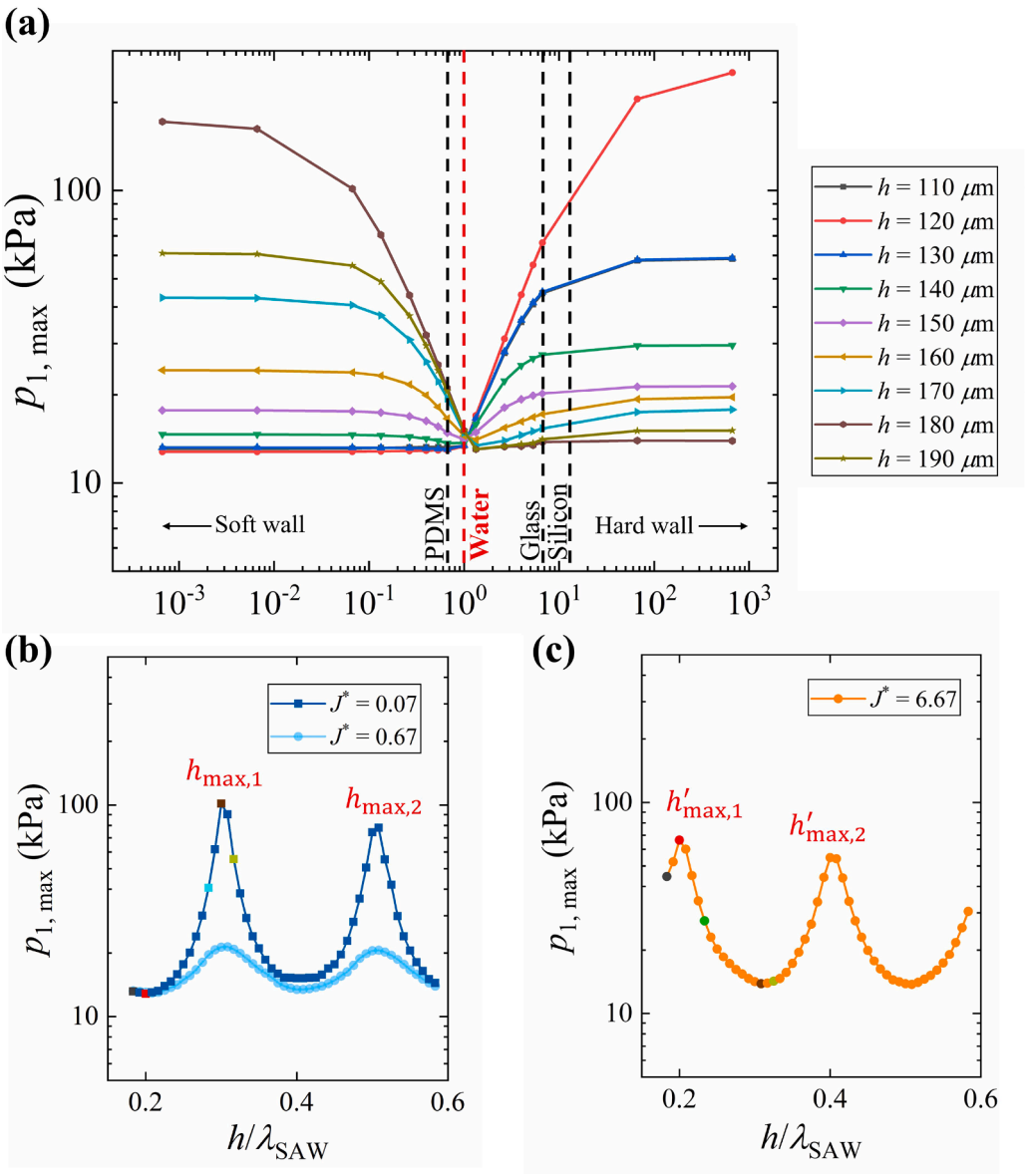

Fig. 6. Variation of acoustic pressure amplitude with the channel height and the acoustic impedance mismatch between the upper channel wall and the fluid. The dashed lines indicate the material of the upper channel wall in the case of a water-filled microchannel.

more than ten times greater than that in scenarios with a low impedance mismatch. This trend levels off as impedance mismatch continues to grow (e.g., $J^* < 10^{-2}$ and $J^* > 10^2$). In contrast, the acoustic energy density increases dramatically with the growing impedance mismatch at channel heights close to $h_{\max,n}$ and $h'_{\max,n}$, while it slightly declines before reaching a plateau when channel heights are significantly outside these ranges. For instance, with channel height of $h = 120\mu$m (which is close to the $h'_{\max,n}$ for $J^* > 1$ and far from $h_{\max,n}$ for $J^* < 1$), as denoted by red line in Fig. 7, a rapid increase in acoustic energy density is observed with widening acoustic impedance mismatch for $J^* > 1$, while a declining trend is noted for $J^* < 1$. Therefore, employing an upper channel wall with a relatively high impedance mismatch has the potential to attain large acoustic pressure amplitude and store significant acoustic energy within the channel fluid.

In Figs. 6**(a)** and 7, we also take into account the influences of the channel height. In the cases of low impedance discrepancy between the upper channel wall and the fluid, the formation of standing waves in the vertical direction is notably weak, rendering little dependence of the interference pattern of the standing wave field and the acoustic pressure amplitude on the channel height. However, as the impedance mismatch increases, the channel height becomes a substantial factor in determining the wave reflection and the interference between incoming and reflected waves. Consequently, the influence of channel height on acoustic pressure amplitude and energy density becomes more pronounced, showcased by the increased discrepancy between the highest amplitude at channel heights of $h'_{\max,n}$ and $h_{\max,n}$ and the lower amplitude at heights beyond these values. Specifically, with a high acoustic impedance mismatch, the acoustic pressure amplitude at different channel heights can vary by an order of magnitude. Hence, selecting the proper channel height is crucial for maximizing the performance of acoustofluidic systems, particularly of those with significant impedance mismatches between the channel wall and the fluid. Our previously outlined formulae for determining the channel heights, $h_{\max,n}$ and $h'_{\max,n}$, can be used to guide device design.

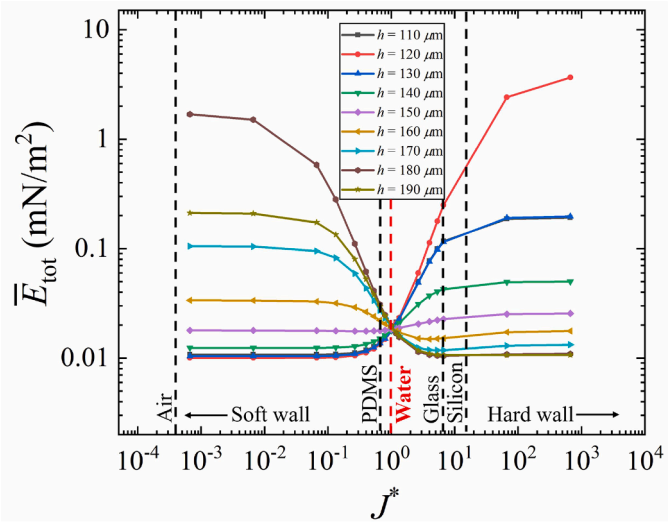

Fig. 7. Spatial average of the total acoustic energy density for different channel height and acoustic impedance mismatch of the upper channel wall and the fluid. The dashed lines indicate the material of the upper channel wall in the case of a water-filled microchannel.

3.2. Acoustophoretic particle aggregation

3.2.1. Aggregation timescale

To evaluate the performance of particle aggregation, the time required for particles to be accumulated is an important indicator. We carried out extensive numerical simulations, tracking the trajectories of particles with an identical radius of 10 μm and examining the aggregation time across various channel heights ranging from 40 to 960 μm and with dimensionless acoustic impedance $J^* = 0.07, 0.67, 6.67$. Fig. 8 illustrates the timescale of particle aggregation, t_a, as a function of the non-dimensional channel height h/λ_{SAW}. The aggregation timescale is defined as the time required for all particles to reach their final equilibrium positions. The optimum channel heights h_{opt}, corresponding to the most efficient particle aggregation characterized by the shortest aggregation time, are marked by red dots and indicated along the horizontal axis with an error less than 5 μm. These optimum channel heights h_{opt} appear periodically at intervals of around $h/\lambda_{SAW} = 0.2$, which can be attributed to the oscillatory variation of acoustic pressure amplitude with channel height as shown in Fig. 6**(b)** and **(c)**. These optimum heights align well with the channel heights $h'_{max,n}$ and $h_{max,n}$ when the acoustic pressure amplitude peaks. Therefore, the dimensionless optimum heights of the microchannel for the bottom-driven acoustofluidic device can be summarized as:

$$h^*_{opt} = \frac{h_{opt}}{\lambda_{SAW}} = \begin{cases} \dfrac{(2n-1)\tan\left[\sin^{-1}\left(\dfrac{c_0}{c_{sub}}\right)\right]}{4}, & J^* < 1 \\ \dfrac{n\tan\left[\sin^{-1}\left(\dfrac{c_0}{c_{sub}}\right)\right]}{2}, & J^* > 1 \end{cases} \tag{20}$$

The formulae account for the acoustic impedance discrepancy between the upper channel wall and the fluid and hold true for all acoustic frequencies, as the height and width of the channel are normalized by the acoustic wavelength. Compared to the longest aggregation time at non-optimum channel heights shown in Fig. 8, optimum channel heights can reduce aggregation time by up to 99 % when $J^* \ll 1$ (176 s at $h = 120\mu$m vs 2 s at $h = 60\mu$m, for $J^* = 0.07$), by a maximum of 76 % when J^* close to 1 (100 s at $h = 120\mu$m vs 23 s at $h = 60\mu$m, for $J^* = 0.67$), and by up to 96 % when $J^* \gg 1$ (150 s at $h = 60\mu$m vs 6 s at $h = 120\mu$m, for $J^* = 6.67$). The significant influence of channel height on aggregation time is further accentuated in scenarios with high acoustic impedance mismatch ($J^* = 0.07$ and 6.67), as shown by the greater fluctuations of the corresponding curves in Fig. 8 than those of the curve representing impedance matching condition ($J^* = 0.67$). Compared to the scenarios with a low acoustic impedance mismatch, a significant acoustic impedance mismatch can achieve up to 91 % reduction in aggregation time at optimum channel height (e.g., 2 s for $J^* = 6.67$ vs 23 s for $J^* = 0.67$, at $h = 60\mu$m), though this advantage gradually diminishes as the channel height increases.

3.2.2. Particle trajectories and final positions

Fig. 9 demonstrates the acoustophoretic motions of polystyrene particles, driven by the combined effects of the acoustic radiation force and the Stokes drag force, with their resultant resting positions denoted by red rectangular boxes. Particles, with a fixed radius of 10μm, are initially evenly distributed within the microchannel. In Fig. 9, particle trajectories and final positions under different dimensionless acoustic impedance J^* are illustrated in different column. With a low acoustic impedance discrepancy between the fluid and the upper channel wall of $J^* = 0.67$ in Fig. 9**(b)**, particles tend to aggregate towards the PNs of the horizontal standing wave, as the standing wave in the vertical direction is relatively weak. Conversely, in cases of high impedance discrepancy shown in Fig. 9**(a)** and **(c)**, except for a few particles near the central regions that are attracted by the horizontal PNs, the majority are directed towards the PNs of the vertical standing wave under the predominant influence of the standing wave component in the vertical direction.

The variations of particle trajectories and velocities with the channel height are illustrated in different rows in Fig. 9. With $J^* = 0.67$ in Fig. 9

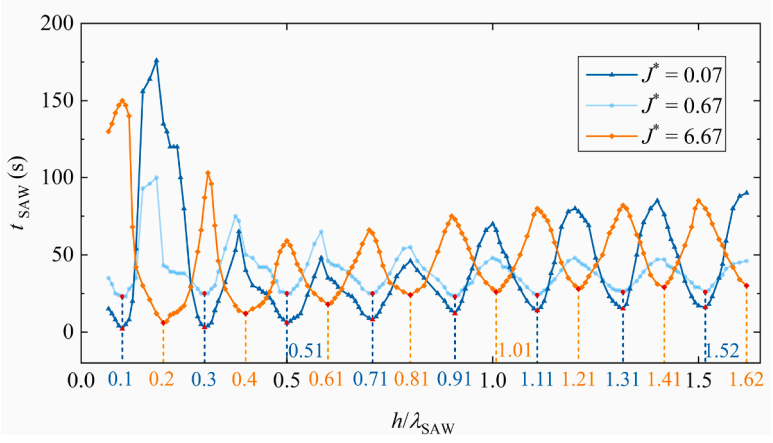

Fig. 8. Timescale for particle aggregation at different channel heights and non-dimensional acoustic impedance J^*.

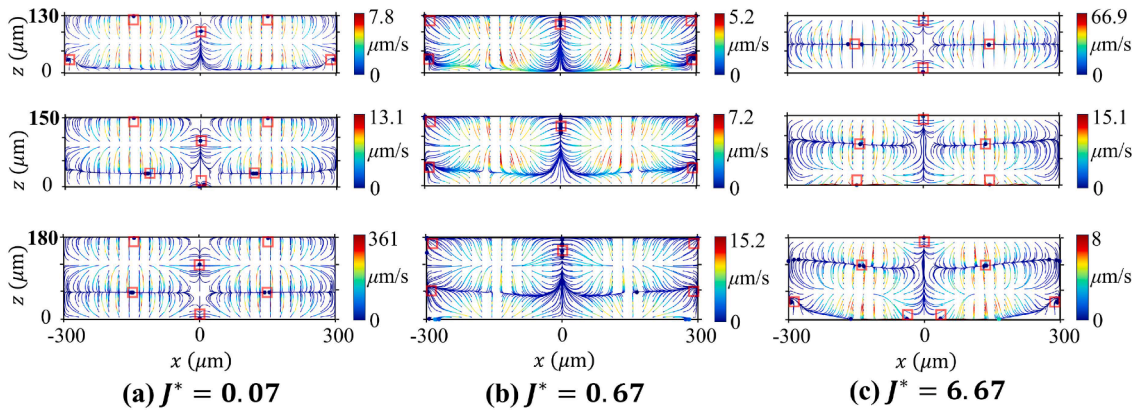

Fig. 9. Particle trajectories and final positions at channel heights of $h = 130\mu$m, $h = 150\mu$m, $h = 180\mu$m and non-dimensional acoustic impedance of J^* = (a) 0.07, (b) 0.67, (c) 6.67. Red boxes indicate the final resting positions of particle aggregation.

(b), particles follow uniform trajectories and eventually accumulate at similar locations, irrespective of the channel height. However, a slight increase in particle velocity is noted as the channel height increases from a non-optimum 130μm to an optimum 180μm. Therefore, in conditions of a low impedance mismatch, the channel height has minor impact on particle trajectories, final positions, and velocities. Conversely, in scenarios with a high acoustic impedance mismatch, such as $J^* = 0.07$ and 6.67 in Fig. 9**(a)** and **(c)**, respectively, particle motions and final resting positions exhibit divergencies during the transition from non-optimum to optimum channel heights. These discrepancies are particularly significant within the lower region of the channel ($z < \lambda_{SAW}/4$) and along its central axis ($x = 0$). Most particles within the upper region of the channel ($z > \lambda_{SAW}/4$) aggregate towards the PNs of the vertical standing wave at $z = h - n\lambda_{\perp}/2$ for $J^* < 1$ and at $z = h - (2n+1)\lambda_{\perp}/4$ for $J^* > 1$ ($n = 0, 1, 2, \ldots$), under the predominant influence of the radiation force, but a few particles near the centre of the channel are drawn towards the PN of the horizontal standing wave at $x = 0$ and terminate at the intersections of the vertical ANs ($z = h - (2n+1)\lambda_{\perp}/4$ for $J^* < 1$ and $z = h - n\lambda_{\perp}/2$ for $J^* > 1$, $n = 0, 1, 2, \ldots$) and horizontal PNs.

As shown in the top row of Fig. 9**(a)**, particles within the lower region of the 130-μm height channel with $J^* = 0.07$ tend to cluster towards horizontal PNs, i.e., sidewalls and centre of the channel, resulting from the pronounced acoustic streaming near the bottom. When the channel height approaches the optimum value to 150 μm, due to the weakened streaming flow, particles within the lower region of the channel tend to migrate towards the intersections of the horizontal ANs ($x = \pm 150\mu$m) and vertical PNs akin to those in the upper region, yet their movement is notably slower and some deviation is observed in their terminal positions. Upon reaching the optimum channel height of 180 μm, particles throughout the channel unanimously converge towards the intersections of the horizontal ANs and vertical PNs at a speed over 50 times greater than that at non-optimum channel heights. Along the central x-axis of the channel, the final position of accumulated particles shifts downwards slightly as the channel height gradually changes to the optimum value, ultimately aligning with the vertical ANs. Similarly, with a non-optimum channel height at $J^* = 6.67$, as illustrated in the bottom two rows of Fig 9**(c)**, particle movements within the lower region are primarily governed by the streaming force, resulting in particles being either propelled towards the two sidewalls or getting trapped and circulated near the bottom. For particles clustered along the centre of the channel, they come to rest at the vertical ANs within a channel of the optimum height, whereas, with a non-optimum channel height, they are pushed upwards all the way to the top of the channel.

3.2.3. Particle tracing on nodal planes

To obtain a better understanding of the underlying mechanisms of particle movements, we decompose the particle velocity $v_{\mathbf{p}}$ into two primary components based on Eq. (12): the radiation force component $v_{\mathbf{rad}} = F_{\mathbf{rad}}/6\pi\mu r$and the streaming component v_2. Figs. 10-12 display the distributions of the magnitude difference between these two velocity components, $v_{\mathbf{diff}} = v_{\mathbf{rad}} - v_2$, with different channel heights and acoustic impedance mismatches between the upper channel wall and the fluid, facilitating the identification of regions dominated by the radiation force (red), the streaming force (blue), and regions where these forces are in balance (white). Pressure nodal planes of horizontal standing wave (HSW) and vertical standing waves (VSW) are represented by blue and green dashed lines, respectively, and small yellow circles indicate the final positions of particles where the difference between the two velocities reaches equilibrium. In addition, the velocity profiles along the pressure nodal planes are depicted in Figs. 10-12 to examine the driving mechanisms of microparticle motion, where green, blue, and blue-green arrows represent particle movements influenced by the streaming force, the radiation force, and both forces, respectively. Red, blue, and green solid lines in velocity profiles correspond to the total particle velocity $v_{\mathbf{p}}$, the x or y components of the radiation velocity $v_{\mathbf{rad}}$, and the x or y components of streaming velocity v_2, respectively.

Fig. 10 depicts the particle velocity profiles and distributions with a dimensionless acoustic impedance $J^* = 0.07$. In Fig. 10**(a)**, distinct pressure nodal planes of HSW and VSW can be observed, denoted by the white regions. As the channel height changes from a non-optimum value of 130μm to an optimum value of 180μm, the nodal plane of VSW gradually shifts upwards from the bottom, so the particle movements to this plane become less affected by the streaming near the bottom boundary. At the optimum channel height, the radiation force pushes the near-bottom particles away from the streaming-dominance region, while at the non-optimum height, particles move towards the bottom and then are trapped inside the streaming vortices. From the velocity profiles along the nodal plane of VSW in Fig. 10**(b)**, particles at a non-optimum channel height of 130μm are seen to be driven towards horizontal PNs mainly governed by the streaming force, while particles at an optimum channel height of 180μm are pushed towards horizontal ANs under the dominant influence of the radiation force. For an intermediate channel height of 150μm, particle motion becomes very slow ($\sim$ 0.05 μm/s) around $x = \pm 220\mu$m due to the small radiation force acting on particles. Hence, it takes quite some time for those particles trapped around $x = \pm 220\mu$m to finally reach their equilibrium positions around $x = \pm 120\mu$m. Regarding particles near the centre of the channel, they initially congregate towards the pressure nodal plane of HSW at the centre of the channel driven by radiation force and subsequently shift to the pressure antinodal planes of VSW. These movements are driven by the streaming force alone at non-optimum channel heights, but by the radiation force at the optimum height, as illustrated in Fig. 10**(c)**. Furthermore, the magnitude of particle velocity at optimum channel heights is up to 30 times greater than that at the non-optimum height,

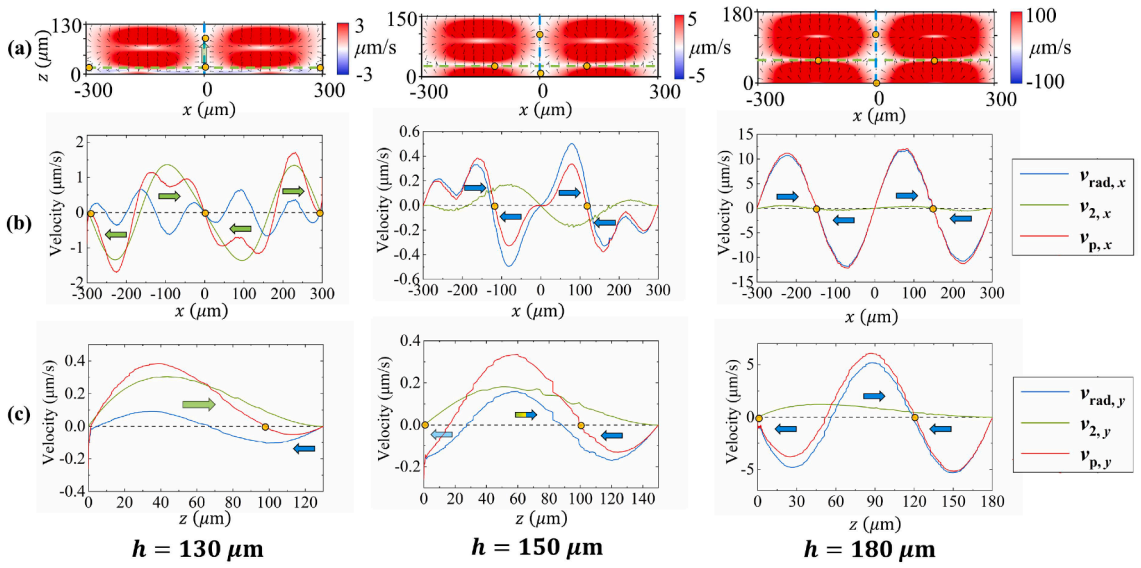

Fig. 10. Particle velocity along pressure nodal planes at non-dimensional acoustic impedance of $J^* = 0.07$ and channel heights of $h = 130\mu$m, $h = 150\mu$m, $h = 180\mu$m. (a) difference between the radiation force component and the streaming component of particle velocity v_{diff}, (b) velocity profile along pressure nodal planes of VSW; (c) velocity profile along pressure nodal planes of HSW.

leading to a more efficient particle aggregation.

In cases where acoustic impedance of the upper wall matches that of the fluid, as shown in Fig. 11, the channel height exerts little influence on the final position and velocity of particles. At a non-optimum channel height of 130μm in Fig. 11**(a)**, as the first pressure nodal plane of VSW is in close proximity to the bottom boundary, the streaming effect is more pronounced, and its influence is comparable to that of the radiation force. Therefore, particles are pushed towards horizontal PNs due to the combined effects of these two forces, as depicted in Fig. 11**(b)**. At the intermediate and optimum channel heights of 150μm and 180μm, respectively, particles' movement towards horizontal PNs is increasingly driven by the radiation force. However, along the pressure nodal plane of HSW at the centre of the channel, since the standing wave is weak in the vertical direction, the magnitude of the radiation force velocity component is relatively small for all the channel heights examined, as shown in Fig. 11**(c)**. Hence, the near-bottom particles are pushed upwards under the dominant influence of the streaming force, while the near-ceiling particles move slightly downwards driven by the radiation force.

For the case of $J^* = 6.67$, Fig. 12 illustrates how particle velocity profiles and distributions vary with the channel height. Contrary to the optimum channel height of 180μm for the case of $J^* < 1$ in Figs 10 and 11, the optimum channel height for the case of $J^* > 1$ is 130μm. At the optimum height of 130μm, the antinodal plane of VSW is located at the bottom, resulting in all near-bottom particles to move upwards, as shown in Fig. 12**(a)**. Subsequently, these particles slide towards the intersections of the pressure antinodal plane of HSW and the pressure nodal plane of VSW, primarily driven by the radiation force, as shown in Fig. 12**(b)**. As the channel height gradually deviates from the optimum value, the first pressure antinodal plane of VSW shifts slightly upwards, leading to the near-bottom particles to be pushed downwards into regions dominated by streaming. Consequently, particle movements along

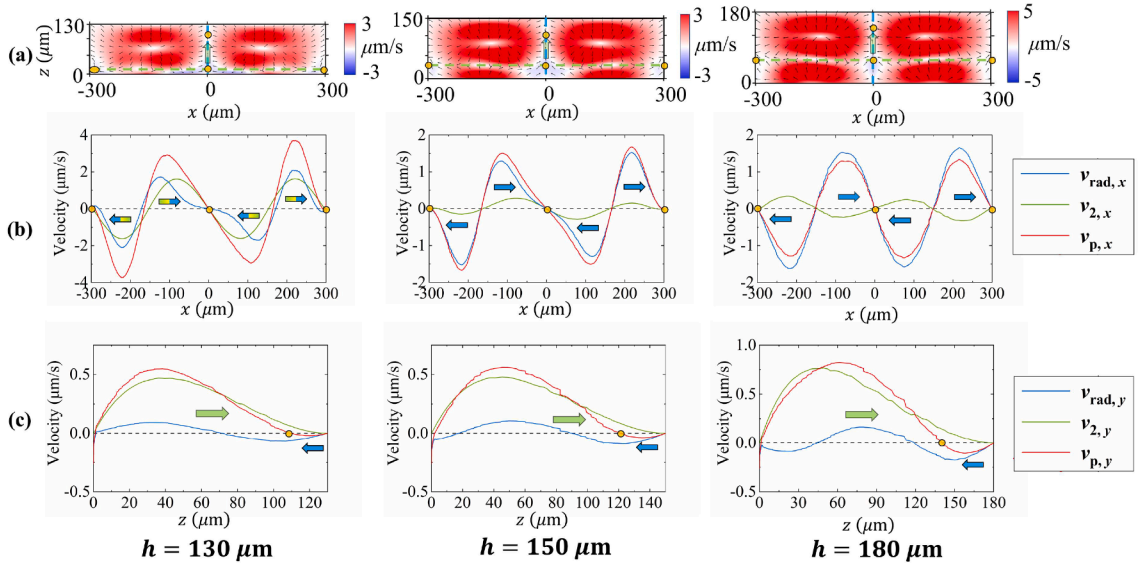

Fig. 11. Particle velocity along pressure nodal planes at non-dimensional acoustic impedance of $J^* = 0.67$ and channel heights of $h = 130\mu$m, $h = 150\mu$m, $h = 180\mu$m. (a) difference between the radiation force component and the streaming component of particle velocity v_{diff}, (b) velocity profile along pressure nodal planes of VSW; (c) velocity profile along pressure nodal planes of HSW.

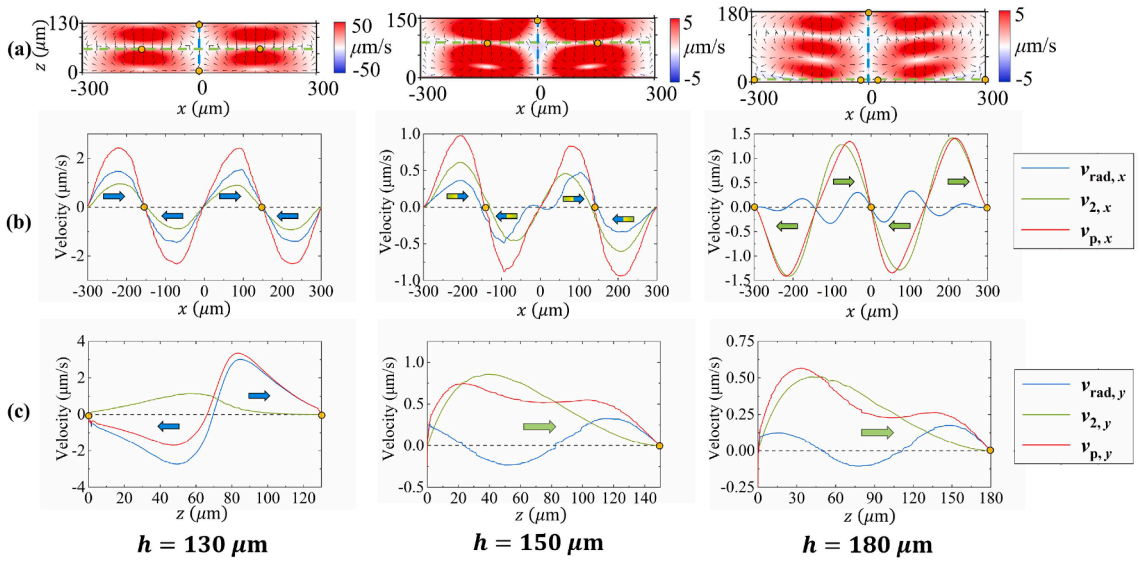

Fig. 12. Particle velocity along pressure nodal planes at non-dimensional acoustic impedance of $J^* = 6.67$ and channel heights of $h = 130\mu$m, $h = 150\mu$m, $h = 180\mu$m. (a) difference between the radiation force component and the streaming component of particle velocity v_{diff}, (b) velocity profile along pressure nodal planes of VSW; (c) velocity profile along pressure nodal planes of HSW.

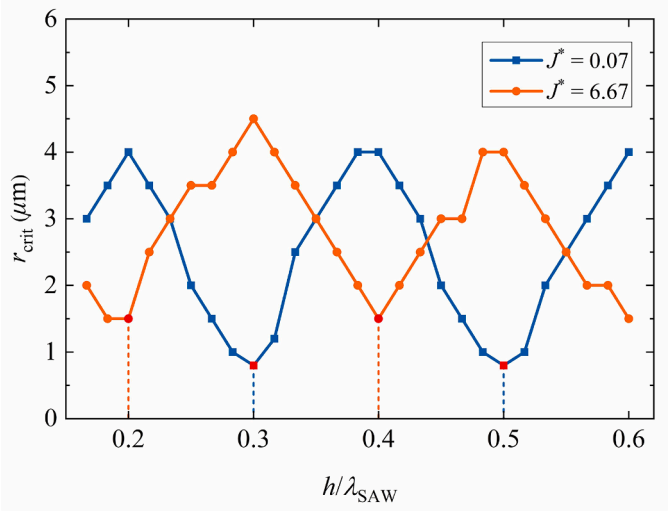

Fig. 13. Threshold radius for particle aggregation at different channel heights and non-dimensional acoustic impedance J^*.

the vertical pressure nodal planes are dominated by the combined effects of both force at a channel height of 150μm and by the streaming force alone at a non-optimum channel height of 180μm, as shown in Fig. 12**(b)**. Along the pressure nodal plane of HSW in Fig. 12**(c)**, particles within the optimum channel move from the centre to the top and bottom of the channel under the influence of the radiation force, while particles within the non-optimum channel are forced by the streaming force all the way to the ceiling of the channel. Similar to the case where $J^* = 0.07$ in Fig. 10, the magnitude of particle velocity varies significantly with the channel height in the case of $J^* = 6.67$, where particle velocity at the optimum channel height can be up to 6 times greater than that at the non-optimum height.

3.3. Particle threshold size

The threshold radius for acoustophoretic aggregation, r_{crit}, is determined for various channel heights and acoustic impedances of the upper channel wall, as shown in Fig. 13. The particle threshold size indicates the transition from streaming-force dominance to radiation-force dominance. From our previous study, the particle threshold radius is around 5 ~ 6 μm for a water-filled PDMS microchannel ($J^* = 0.67$), irrespective of the channel height [34]. In contrast, when the acoustic impedance discrepancy between the upper channel wall and the fluid is significant, the threshold size not only reduces but also exhibits an oscillatory variation with the channel height. At optimum channel heights, marked by red dots in Fig. 13, the threshold radius reaches its minimum, approximately one-fifth of the size at the undesirable channel height (e.g., 4μm at $h = 120\mu$m vs 0.8μm at $h = 180\mu$m, for $J^* = 0.07$). Therefore, by carefully adjusting the channel height and the acoustic impedance mismatch between upper channel wall and the fluid, the threshold size of microparticles can be decreased by an order of magnitude, greatly widening the application of the acoustofluidic device.

Figs. 14-15 demonstrate the representative particle trajectories and the differences between two particle velocity components, v_{diff}, at non-optimum and optimum channel heights, respectively. Here, the dimensionless acoustic impedance is fixed at $J^* = 0.07$. The acoustophoretic particle trajectory strongly depends on the particle size. The below-threshold particles, such as 1μm particles in a 240-μm-high channel in Fig. 14**(a)** and 0.2μm particles in a 300-μm-high channel in Fig. 15**(a)**, are caught in streaming vortices due to the dominance of the viscous drag force. In contrast, the above-threshold particles, such as 8μm particles in a 240-μm-high channel in Fig. 14**(d)** and 2μm particles in a 300-μm-high channel in Fig. 15**(d)**, are pushed towards PNs due to the dominance of the radiation force. As the particle radius approaches the threshold value in Figs. 14**(b)** and 15**(b)**, a distinct aggregation pattern exhibits, as the dominant force switches in different locations of the channel. Particles in the bottom region of the channel ($z < \lambda_{\text{SAW}}/4 = 150\mu$m) keep circulating within streaming vortices, ultimately accumulating at the centre of these vortices, whereas particles within the upper region of the channel slowly shift towards the PNs. This behaviour is consistent with the spatial variation of particle velocity components. The streaming velocity component mainly dominate the bottom region of the channel, whereas the radiation velocity component governs the upper region. Once the particle radius reaches the threshold value, this spatially uneven aggregation pattern vanishes, and all particles are pushed towards PNs by the radiation force, as depicted in Figs. 14**(c)** and 15**(c)**. While the streaming force may exert dominance in certain spots near the bottom, as denoted by the blue areas in Figs. 14**(c)** and 15**(c)**, its

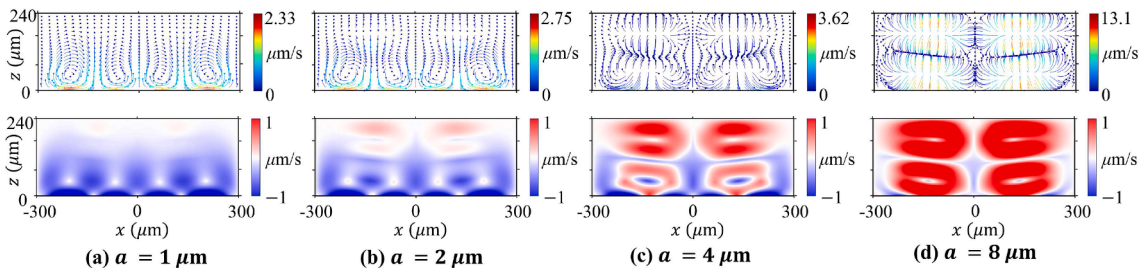

Fig. 14. Particle trajectories and distributions of difference between the radiation force component and the streaming component of particle velocity v_{diff} at non-optimum channel height of $h = 240\mu$m and non-dimensional acoustic impedance of $J^* = 0.07$ for particle radii of (a) 1, (b) 2, (c) 4, (d) 8 μm.

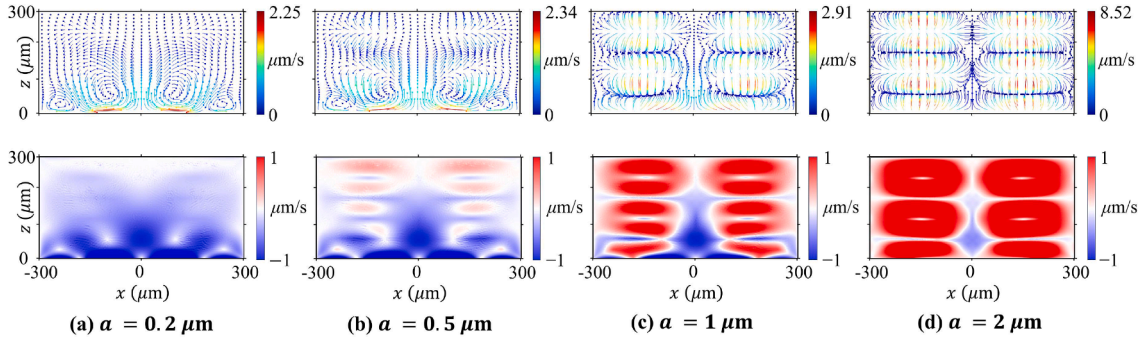

Fig. 15. Particle trajectories and distributions of difference between the radiation force component and the streaming component of particle velocity at optimum channel height of $h = 300\mu$m and non-dimensional acoustic impedance of $J^* = 0.07$ for particle radii of (a) 0.2, (b) 0.5, (c) 1, (d) 2 μm.

overall influence on particle trajectories is minor in shaping the aggregation pattern.

4. Discussion

In this work, we established a full model of acoustofluidic devices that incorporates piezoelectricity in the substrate, acoustics in the microchannel wall, and fluid dynamics in the fluid cavity. The numerical model has been validated against the numerical and experimental results reported by Sun et al. [52], and the acoustic field, induced second-order flow field, and particle movement were simulated. The influences of the height and acoustic impedance of the microchannel lid on the acoustofluidic fields and the acoustophoretic motion were extensively studied, aiming at determining the optimum design parameters for rapid microparticle aggregation.

We found that a significant mismatch in acoustic impedance between the upper channel wall and the fluid can amplify the acoustic pressure field by more than an order of magnitude than that a perfectly impedance-matched microchannel. Unlike scenarios with little acoustic impedance mismatch, the channel height greatly affects the acoustic pressure amplitude when there is a significant impedance mismatch, exhibiting up to a tenfold difference. Furthermore, by increasing acoustic impedance mismatch and optimising the channel height, the aggregation time can be reduced by up to 91 % compared to the low impedance-mismatch case. Based on our previous study [34], we have developed a normalized formula for determining the optimum channel height, including scenarios where the acoustic impedance of the upper wall is either greater than or smaller than that of the fluid.

In addition, we conducted extensive numerical simulations of microparticle trajectories to characterize their movements and identify their final resting positions and threshold sizes. In contrast to behaviours observed in impedance-matched PDMS channels, where particles tend to aggregate towards PNs of the horizontal standing waves, particles in channels with a significant acoustic impedance mismatch are observed to accumulate at the intersections of the ANs of horizontal standing waves and the PNs of vertical standing waves. We analysed the spatial variation of the difference between the radiation force and the viscous drag force, providing insights into the particle movements. Our findings also revealed a dependence of particle threshold size on the channel height in cases of significant impedance mismatch between the channel wall and the fluid. The average threshold size is approximately four times smaller than that observed in impedance-matched conditions, and the smallest threshold size achieved herein is 1.6 μm.

In conclusion, great advantages can be gained by finetuning the height and acoustic properties of the channel wall of acoustofluidic device. This work provides valuable guidelines for the device design and optimization, facilitating the wider and more efficient application of acoustophoretic aggregation.

CRediT authorship contribution statement

Yiming Li: Writing – original draft, Visualization, Software, Methodology, Investigation, Formal analysis, Data curation, Conceptualization. **Dongfang Liang:** Writing – review & editing, Visualization, Supervision, Resources, Methodology, Funding acquisition, Formal analysis. **Alexandre Kabla:** Writing – review & editing, Visualization. **Yuning Zhang:** Writing – review & editing, Visualization. **Jun Ma:** Writing – review & editing. **Xin Yang:** Writing – review & editing, Visualization, Resources.

Declaration of competing interest

The authors declare that they have no known competing financial interests or personal relationships that could have appeared to influence the work reported in this paper.

Acknowledgements

We are grateful to the financial support by EPSRC (Grant Number EP/N021614/1) and the Cambridge Tsinghua Joint Research Initiative Fund.

Data availability

The data that support the findings of this study are available from the corresponding author upon reasonable request.

References

[1] S. Zhou, B. Chen, E.S. Fu, H. Yan, Computer vision meets microfluidics: a label-free method for high-throughput cell analysis, Microsyst. Nanoeng. 9 (1) (2023) 1–15, https://doi.org/10.1038/s41378-023-00562-8.

[2] X. Xu, et al., Digital microfluidics for biological analysis and applications, Lab. Chip 23 (5) (2023) 1169–1191, https://doi.org/10.1039/D2LC00756H.

[3] J.A. Lombardo, M. Aliaghaei, Q.H. Nguyen, K. Kessenbrock, J.B. Haun, Microfluidic platform accelerates tissue processing into single cells for molecular analysis and primary culture models, Nat. Commun. 12 (1) (2021) 2858, https://doi.org/10.1038/s41467-021-23238-1.

[4] G. Velve-Casquillas, M. Le Berre, M. Piel, P.T. Tran, Microfluidic tools for cell biological research, Nano Today 5 (1) (2010) 28–47, https://doi.org/10.1016/j.nantod.2009.12.001.

[5] Y. Xie, L. Dai, Y. Yang, Microfluidic technology and its application in the point-of-care testing field, Biosens. Bioelectron. X 10 (2022) 100109, https://doi.org/10.1016/j.biosx.2022.100109.

[6] P. Yager, et al., Microfluidic diagnostic technologies for global public health, Nature 442 (7101) (2006) 412–418, https://doi.org/10.1038/nature05064.

[7] P.S. Dittrich, A. Manz, Lab-on-a-chip: microfluidics in drug discovery, Nat. Rev. Drug Discov. 5 (3) (2006) 210–218, https://doi.org/10.1038/nrd1985.

[8] Y. Liu, X. Jiang, Why microfluidics? Merits and trends in chemical synthesis, Lab. Chip 17 (23) (2017) 3960–3978, https://doi.org/10.1039/C7LC00627F.

[9] X. Xuan, Recent advances in direct current electrokinetic manipulation of particles for microfluidic applications, ELECTROPHORESIS (2019), https://doi.org/10.1002/elps.201900048.

[10] J. Rufo, F. Cai, J. Friend, M. Wiklund, T.J. Huang, Acoustofluidics for biomedical applications, Nat. Rev. Methods Primer 2 (1) (2022) 30, https://doi.org/10.1038/s43586-022-00109-7.

[11] F. Tian, Z. Han, J. Deng, C. Liu, J. Sun, Thermomicrofluidics for biosensing applications, VIEW 2 (6) (2021) 20200148, https://doi.org/10.1002/VIW.20200148.

[12] R.-J. Yang, H.-H. Hou, Y.-N. Wang, L.-M. Fu, Micro-magnetofluidics in microfluidic systems: A review, Sens. Actuators B Chem. 224 (2016) 1–15, https://doi.org/10.1016/j.snb.2015.10.053.

[13] T. Peng, C. Fan, M. Zhou, F. Jiang, D. Drummer, B. Jiang, Rapid enrichment of submicron particles within a spinning droplet driven by a unidirectional acoustic transducer, Anal. Chem. 93 (39) (2021) 13293–13301, https://doi.org/10.1021/acs.analchem.1c02914.

[14] Y. Gu, et al., Acoustofluidic centrifuge for nanoparticle enrichment and separation, Sci. Adv. 7 (1) (2021) eabc0467, https://doi.org/10.1126/sciadv.abc0467.

[15] P. Dumčius et al., 'Dual-wave acoustofluidic centrifuge for ultrafast concentration of nanoparticles and extracellular vesicles', *Small*, vol. n/a, no. n/a, p. 2300390, doi: 10.1002/smll.202300390.

[16] L. Shen, et al., Acousto-dielectric tweezers enable independent manipulation of multiple particles, Sci. Adv. 10 (32) (2024) eado8992, https://doi.org/10.1126/sciadv.ado8992.

[17] L. Shen, et al., Joint subarray acoustic tweezers enable controllable cell translation, rotation, and deformation, Nat. Commun. 15 (1) (2024) 9059, https://doi.org/10.1038/s41467-024-52686-8.

[18] P. Li, et al., Acoustic separation of circulating tumor cells, Proc. Natl. Acad. Sci. 112 (16) (2015) 4970–4975, https://doi.org/10.1073/pnas.1504484112.

[19] Z. Wu, et al., The acoustofluidic focusing and separation of rare tumor cells using transparent lithium niobate transducers, Lab. Chip 19 (23) (2019) 3922–3930, https://doi.org/10.1039/C9LC00874H.

[20] M. Wu, et al., Isolation of exosomes from whole blood by integrating acoustics and microfluidics, Proc. Natl. Acad. Sci. 114 (40) (2017) 10584–10589, https://doi.org/10.1073/pnas.1709210114.

[21] P.-H. Huang, et al., An acoustofluidic sputum liquefier, Lab. Chip 15 (15) (2015) 3125–3131, https://doi.org/10.1039/C5LC00539F.

[22] Y.Q. Fu, et al., Advances in piezoelectric thin films for acoustic biosensors, acoustofluidics and lab-on-chip applications, Prog. Mater. Sci. 89 (2017) 31–91, https://doi.org/10.1016/j.pmatsci.2017.04.006.

[23] P.B. Muller, R. Barnkob, M.J.H. Jensen, H. Bruus, A numerical study of microparticle acoustophoresis driven by acoustic radiation forces and streaming-induced drag forces, Lab. Chip 12 (22) (2012) 4617, https://doi.org/10.1039/c2lc40612h.

[24] I. Leibacher, S. Schatzer, J. Dual, Impedance matched channel walls in acoustofluidic systems, Lab Chip 14 (3) (2014) 463–470, https://doi.org/10.1039/C3LC51109J.

[25] M.A. Şahin, B. Çetin, M.B. Özer, Investigation of effect of design and operating parameters on acoustophoretic particle separation via 3D device-level simulations, Microfluid. Nanofluidics 24 (1) (2019) 8, https://doi.org/10.1007/s10404-019-2311-1.

[26] S. Marefati, M. Ghassemi, V. Ghazizadeh, Investigation of effective parameters on streaming-induced acoustophoretic particle manipulation in a microchannel via three-dimensional numerical simulation, Phys. Fluids 34 (1) (2022) 012008, https://doi.org/10.1063/5.0077392.

[27] H.N. Açıkgöz, et al., Assessment of silicon, glass, FR4, PDMS and PMMA as a chip material for acoustic particle/cell manipulation in microfluidics, Ultrasonics 129 (2023) 106911, https://doi.org/10.1016/j.ultras.2022.106911.

[28] S. Maramizonouz, et al., Acoustofluidic patterning inside capillary tubes using standing surface acoustic waves, Int. J. Mech. Sci. 214 (2022) 106893, https://doi.org/10.1016/j.ijmecsci.2021.106893.

[29] S. Zhao, et al., A disposable acoustofluidic chip for nano/microparticle separation using unidirectional acoustic transducers, Lab. Chip 20 (7) (2020) 1298–1308, https://doi.org/10.1039/D0LC00106F.

[30] H.G. Kraus, Huygens–Fresnel–Kirchhoff wave-front diffraction formulation: spherical waves, J. Opt. Soc. Am. A 6 (8) (1989) 1196, https://doi.org/10.1364/JOSAA.6.001196.

[31] D.J. Collins, R. O'Rorke, A. Neild, J. Han, Y. Ai, Acoustic fields and microfluidic patterning around embedded micro-structures subject to surface acoustic waves, Soft Matter 15 (43) (2019) 8691–8705, https://doi.org/10.1039/C9SM00946A.

[32] R. O'Rorke, D. Collins, Y. Ai, A rapid and meshless analytical model of acoustofluidic pressure fields for waveguide design, Biomicrofluidics 12 (2) (2018) 024104, https://doi.org/10.1063/1.5021117.

[33] Z. Tian, et al., Wave number–spiral acoustic tweezers for dynamic and reconfigurable manipulation of particles and cells, Sci. Adv. 5 (5) (2019) eaau6062, https://doi.org/10.1126/sciadv.aau6062.

[34] Y. Li, D. Liang, A. Kabla, Y. Zhang, X. Yang, Sensitivity of acoustofluidic particle manipulation to microchannel height in standing surface acoustic wave-based microfluidic devices, Phys. Fluids 35 (12) (2023) 122018, https://doi.org/10.1063/5.0177118.

[35] H. Wang, et al., Modelling hybrid acoustofluidic devices for enhancing Nano- and Micro-Particle manipulation in microfluidics, Appl. Acoust. 205 (2023) 109258, https://doi.org/10.1016/j.apacoust.2023.109258.

[36] M. Wu, et al., High-throughput cell focusing and separation *via* acoustofluidic tweezers, Lab. Chip 18 (19) (2018) 3003–3010, https://doi.org/10.1039/C8LC00434J.

[37] M. Wu, et al., Circulating tumor cell phenotyping via high-throughput acoustic separation, Small 14 (32) (2018) 1801131, https://doi.org/10.1002/smll.201801131.

[38] J. Dual, D. Möller, Acoustofluidics 4: Piezoelectricity and application in the excitation of acoustic fields for ultrasonic particle manipulation, Lab. Chip 12 (3) (2012) 506, https://doi.org/10.1039/c1lc20913b.

[39] M.S. Namnabat, M.Moghimi Zand, E. Houshfar, 3D numerical simulation of acoustophoretic motion induced by boundary-driven acoustic streaming in standing surface acoustic wave microfluidics, Sci. Rep. 11 (1) (2021) 13326, https://doi.org/10.1038/s41598-021-90825-z.

[40] J.-C. Hsu, C.-L. Chao, Full-wave modeling of micro-acoustofluidic devices driven by standing surface acoustic waves for microparticle acoustophoresis, J. Appl. Phys. 128 (12) (2020) 124502, https://doi.org/10.1063/5.0017933.

[41] H. Bruus, Acoustofluidics 2: Perturbation theory and ultrasound resonance modes, Lab Chip 12 (1) (2012) 20–28, https://doi.org/10.1039/C1LC20770A.

[42] H. Bruus, Acoustofluidics 7: The acoustic radiation force on small particles, Lab. Chip 12 (6) (2012) 1014, https://doi.org/10.1039/c2lc21068a.

[43] M. Settnes, H. Bruus, Forces acting on a small particle in an acoustical field in a viscous fluid, Phys. Rev. E 85 (1) (2012) 016327, https://doi.org/10.1103/PhysRevE.85.016327.

[44] M.W.H. Ley, H. Bruus, Three-dimensional numerical modeling of acoustic trapping in glass capillaries, Phys. Rev. Appl. 8 (2) (2017) 024020, https://doi.org/10.1103/PhysRevApplied.8.024020.

[45] R.P. Moiseyenko, H. Bruus, Whole-SYSTEM ULTRASOUND RESONANCES AS THE BASIS FOR Acoustophoresis in All-polymer microfluidic devices, Phys. Rev. Appl. 11 (1) (2019) 014014, https://doi.org/10.1103/PhysRevApplied.11.014014.

[46] N. Nama, R. Barnkob, Z. Mao, C.J. Kähler, F. Costanzo, T.J. Huang, Numerical study of acoustophoretic motion of particles in a PDMS microchannel driven by surface acoustic waves, Lab. Chip 15 (12) (2015) 2700–2709, https://doi.org/10.1039/C5LC00231A.

[47] P.B. Muller, R. Barnkob, M.J.H. Jensen, H. Bruus, A numerical study of microparticle acoustophoresis driven by acoustic radiation forces and streaming-induced drag forces, Lab. Chip 12 (22) (2012) 4617, https://doi.org/10.1039/c2lc40612h.

[48] L.D. Landau, E.M. Lifshitz, J.B. Sykes, W.H. Reid, E.H. Dill, Theory of elasticity: Vol. 7 of Course of theoretical physics, Phys. Today 13 (7) (1960) 44–46, https://doi.org/10.1063/1.3057037.

[49] M.J. Holmes, N.G. Parker, M.J.W. Povey, Temperature dependence of bulk viscosity in water using acoustic spectroscopy, J. Phys. Conf. Ser. 269 (2011) 012011, https://doi.org/10.1088/1742-6596/269/1/012011.

[50] I. Kuznetsova, et al., The peculiarities of the acoustic waves of zero-order focusing in lithium Niobate Plate, Sensors 21 (12) (2021) 4000, https://doi.org/10.3390/s21124000.

[51] D. R. Lide, G. Baysinger, S. Chemistry, L. I. Berger, R. N. Goldberg, and H. V. Kehiaian, 'CRC Handbook of Chemistry and Physics', p. 2661.

[52] C. Sun, et al., Gallium nitride: a versatile compound semiconductor as novel piezoelectric film for acoustic tweezer in manipulation of cancer cells, IEEE Trans. Electron Devices 67 (8) (2020) 3355–3361, https://doi.org/10.1109/TED.2020.3002498.